**SUPPORTING INFORMATION**

# Experimental and Theoretical Assessments of Aluminum Proximity in MFI Zeolites and its Alteration by Organic and Inorganic Structure-Directing Agents

Claire T. Nimlos[1,†], Alexander J. Hoffman[2,†], Young Gul Hur[1], Byung Jin Lee[1,3], John R. Di Iorio[1], David D. Hibbitts[2,*], and Rajamani Gounder[1,*]

[1]*Charles D. Davidson School of Chemical Engineering, Purdue University, 480 Stadium Mall Drive, West Lafayette, IN 47907, USA*

[2]*Department of Chemical Engineering, University of Florida, 1030 Center Drive, Gainesville, FL 32611, USA*

[3]*Department of Chemical and Biological Engineering, Korea University, 145 Anam-ro, Seongbuk-gu, Seoul 02841, Republic of Korea*

[†]C. T. N. and A. J. H. contributed equally to this work.

*Corresponding authors. E-mails: hibbitts@ufl.edu, rgounder@purdue.edu

# Table of Contents

**Section S1. XRD Patterns of MFI Samples**

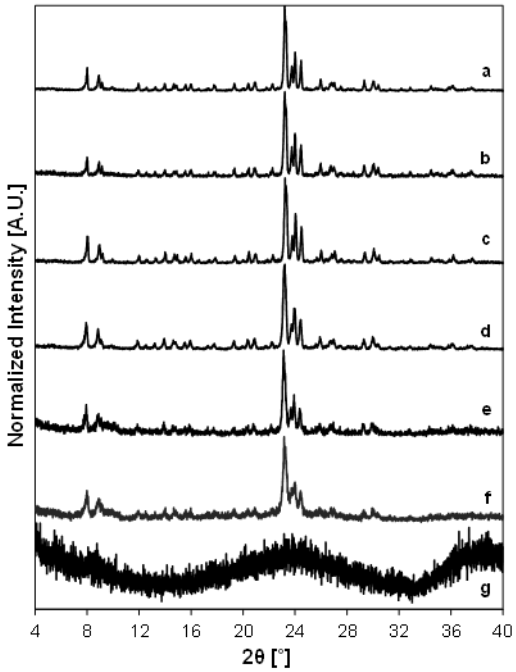


**Figure S1.** XRD patterns of MFI samples synthesized with only $TPA^+$ as the SDA. (a) MFI-TPA(185,0), (b) MFI-TPA(159,0), (c) MFI-TPA(118,0), (d) MFI-TPA(71,0), (e) MFI-TPA(50,0), (f) MFI-TPA(37,0), (g) sample synthesized with a gel Si/Al = 30 was amorphous after 7d (433 K).

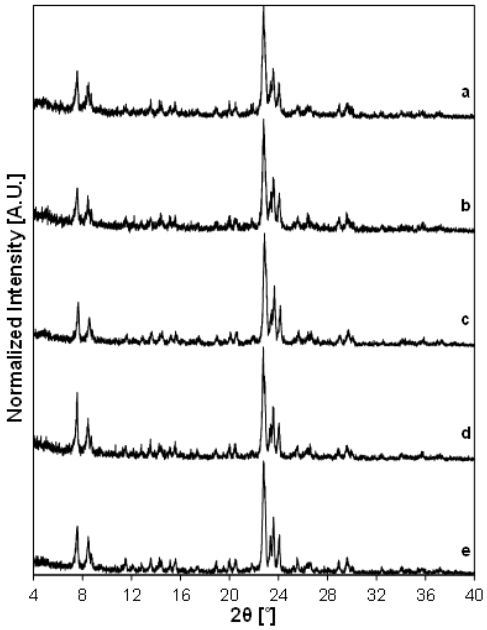


**Figure S2.** XRD patterns of MFI samples synthesized with $TPA^+$ and $Na^+$ as co-SDAs with a gel Si/Al = 50. (a) MFI-TPA(52,0.25), (b) MFI-TPA(57,0.75), (c) MFI-TPA(51,1.5), (d) MFI-TPA(58,3), (e) MFI-TPA(55,5).

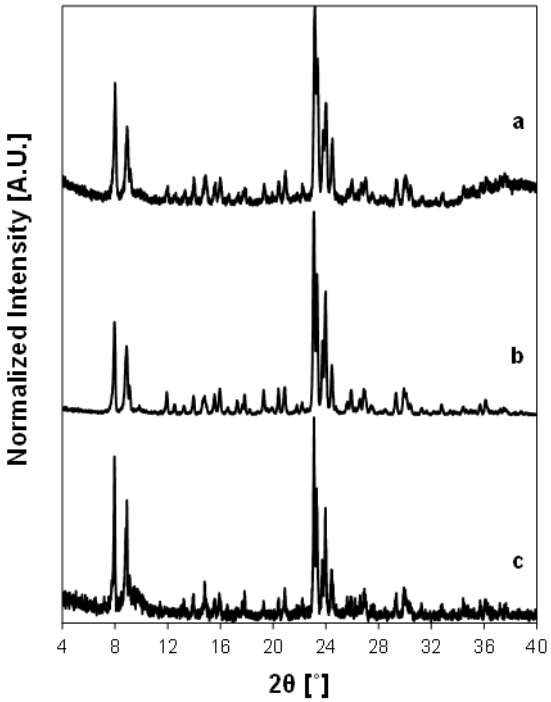


**Figure S3.** XRD patterns of MFI samples synthesized with neutral OSDAs. (a) MFI-PETP(43,0.5), (b) MFI-DABCO(44,0.04)-1, (c) MFI-DABCO(44,0.04)-2.

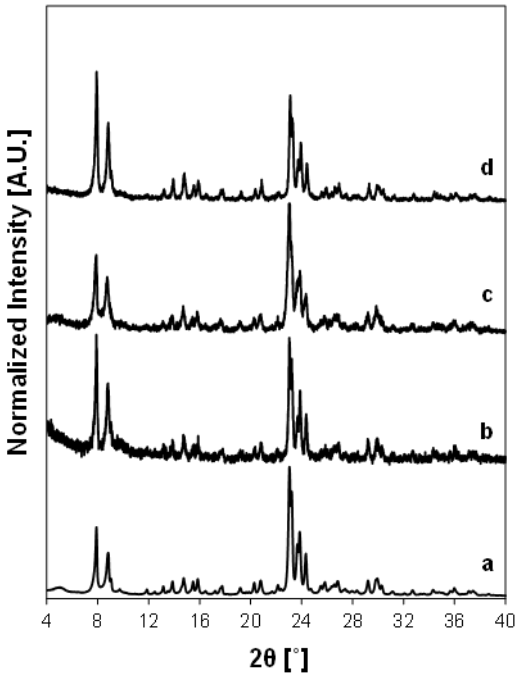


**Figure S4.** XRD patterns of commercial MFI samples from Zeolyst. (a) MFI(13,C), (b) MFI(17,C), (c) MFI(31,C), (d) MFI(43,C).

**Section S2. $N_2$ Adsorption Isotherms of MFI Samples**

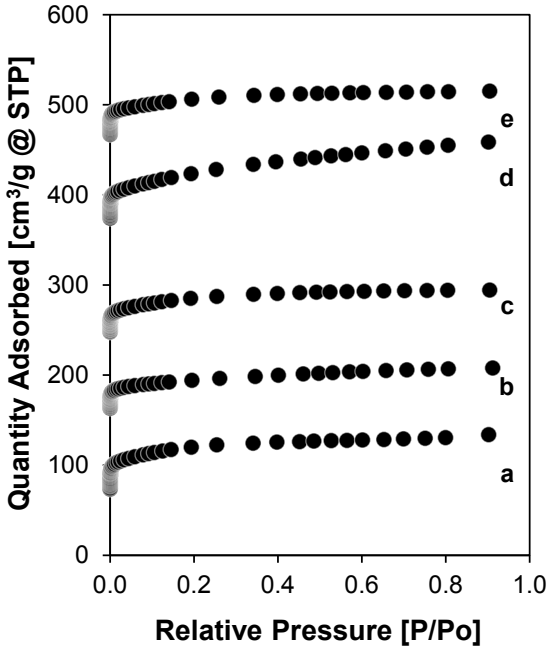


**Figure S5.** $N_2$ adsorption isotherms (77 K) of MFI samples synthesized with only $TPA^+$ as the SDA. (a) MFI-TPA(185,0), (b) MFI-TPA(159,0), (c) MFI-TPA(118,0), (d) MFI-TPA(71,0), (e) MFI-TPA(50,0). Isotherms vertically offset by 100 $cm^3\ g^{-1}$ @ STP for clarity.

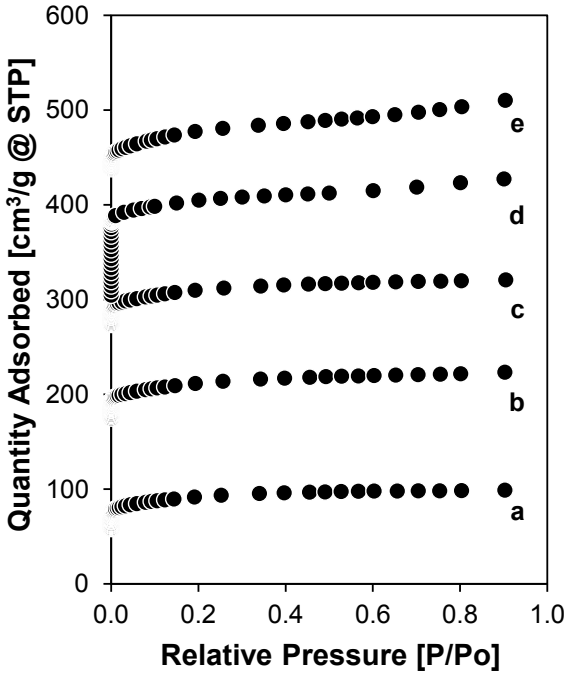


**Figure S6.** $N_2$ adsorption isotherms (77 K) of MFI samples synthesized with $TPA^+$ and $Na^+$ as co-SDAs at a gel Si/Al = 50. (a) MFI-TPA(52,0.25), (b) MFI-TPA(57,0.75), (c) MFI-TPA(51,1.5), (d) MFI-TPA(58,3), (e) MFI-TPA(55,5). Isotherms vertically offset by 100 $cm^3\ g^{-1}$ @ STP for clarity.

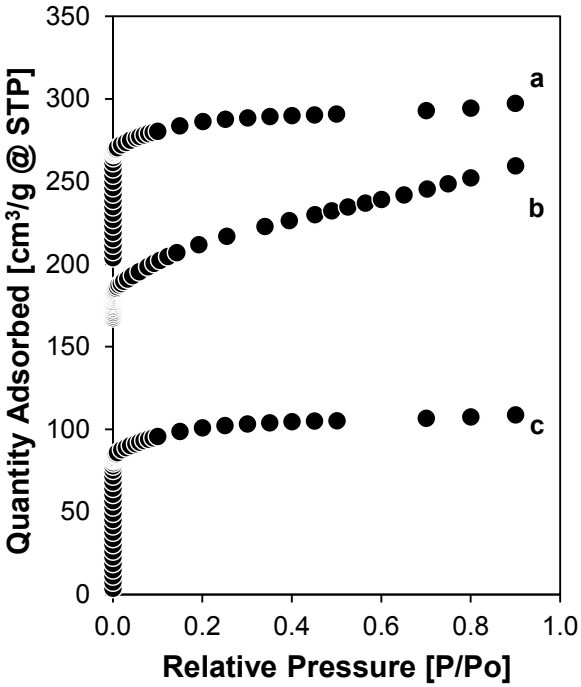


**Figure S7.** $N_2$ adsorption isotherms (77 K) of MFI samples synthesized with neutral OSDAs. (a) MFI-PETP(43,0.5), (b) MFI-DABCO(44,0.04)-1, (c) MFI-DABCO(44,0.04)-2. Isotherms vertically offset by 100 $cm^3\ g^{-1}$ @ STP for clarity.

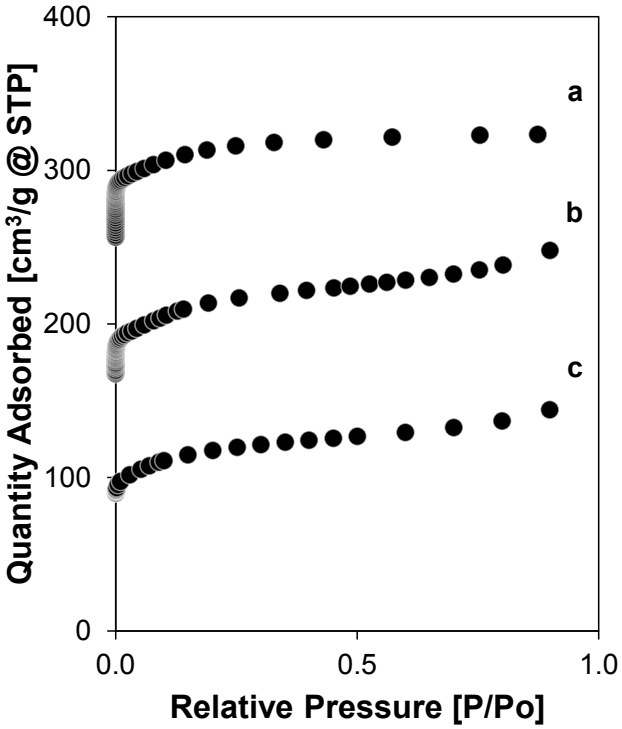


**Figure S8.** $N_2$ adsorption isotherms (77 K) of commercial MFI samples. (a) MFI(13,C), (b) MFI(17,C), (c) MFI(43,C). Isotherms vertically offset by 100 $cm^3\ g^{-1}$ @ STP for clarity.

**Section S3. $^{27}$Al MAS NMR of MFI Samples**

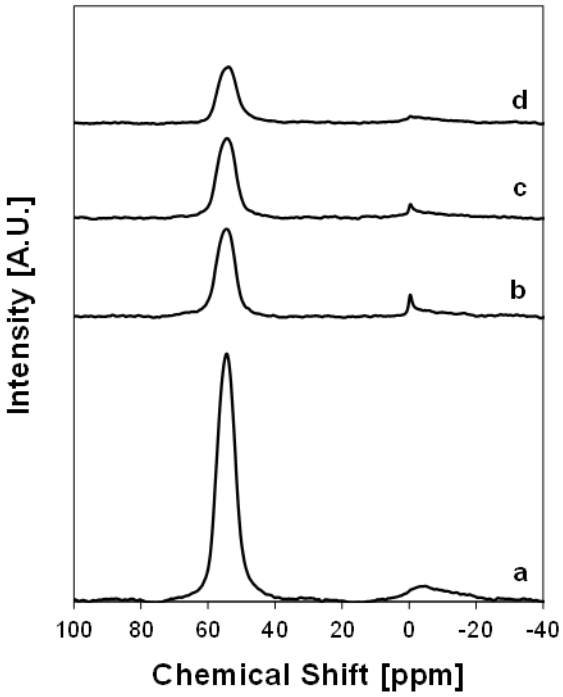


**Figure S9.** $^{27}$Al MAS NMR spectra on (a) MFI-TPA(50,0), (b) MFI-TPA(118,0), (c) MFI-TPA(159,0), (d) MFI-TPA(185,0). Spectra vertically offset for clarity.

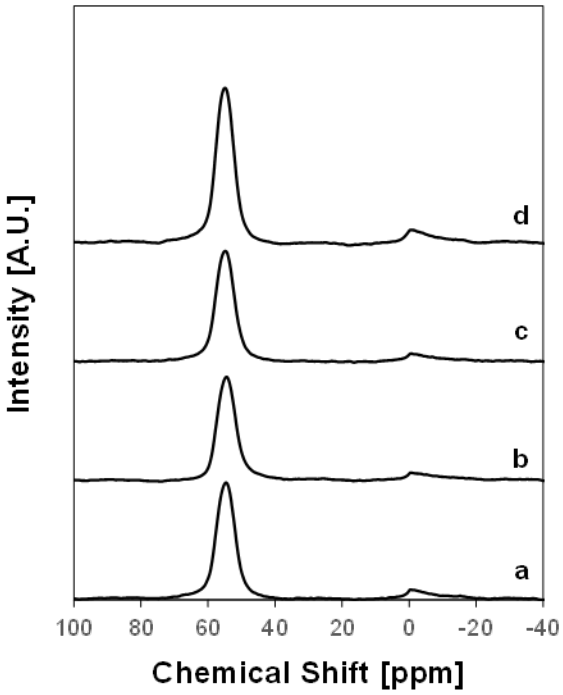


**Figure S10.** $^{27}$Al MAS NMR spectra on (a) MFI-TPA(50,0.75), (b) MFI-TPA(51,1.5), (c) MFI-TPA(58,3), (d) MFI-TPA(55,5). Spectra vertically offset for clarity.

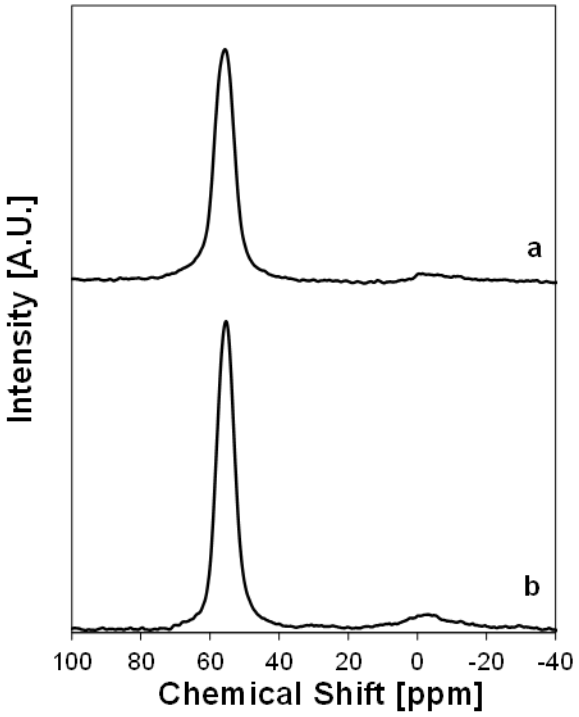


**Figure S11.** $^{27}$Al MAS NMR spectra on (a) MFI-DABCO(44,0.04)-1, (b) MFI-PETP(43,0.5). Spectra vertically offset for clarity.

**Table S1.** Estimate of percentage of $Al_f$ (resonance at 55 ppm) and $Al_{ex}$ (resonance at 0 ppm) from $^{27}$Al MAS NMR spectra of each sample.

| Sample | $Al_f$ (%) | $Al_{ex}$ (%) |
|---|---|---|
| MFI-TPA(37,0) | – | – |
| MFI-TPA(50,0) | 93 | 7 |
| MFI-TPA(71,0) | – | – |
| MFI-TPA(118,0) | 86 | 14 |
| MFI-TPA(159,0) | 87 | 13 |
| MFI-TPA(185,0) | 92 | 8 |
| MFI-TPA (52,0.25) | – | – |
| MFI-TPA(57,0.75) | 96 | 4 |
| MFI-TPA(51,1.5) | 94 | 6 |
| MFI-TPA(58,3) | 97 | 3 |
| MFI-TPA(55,5) | 95 | 5 |
| MFI-PETP(43,0.5) | 92 | 8 |
| MFI-DABCO(44,0.04)-1 | 89 | 11 |
| MFI-DABCO(44,0.04)-2 | – | – |

**Section S4. $NH_3$ TPD of $NH_4$- and Co-form MFI Samples to Quantify Acid Sites**

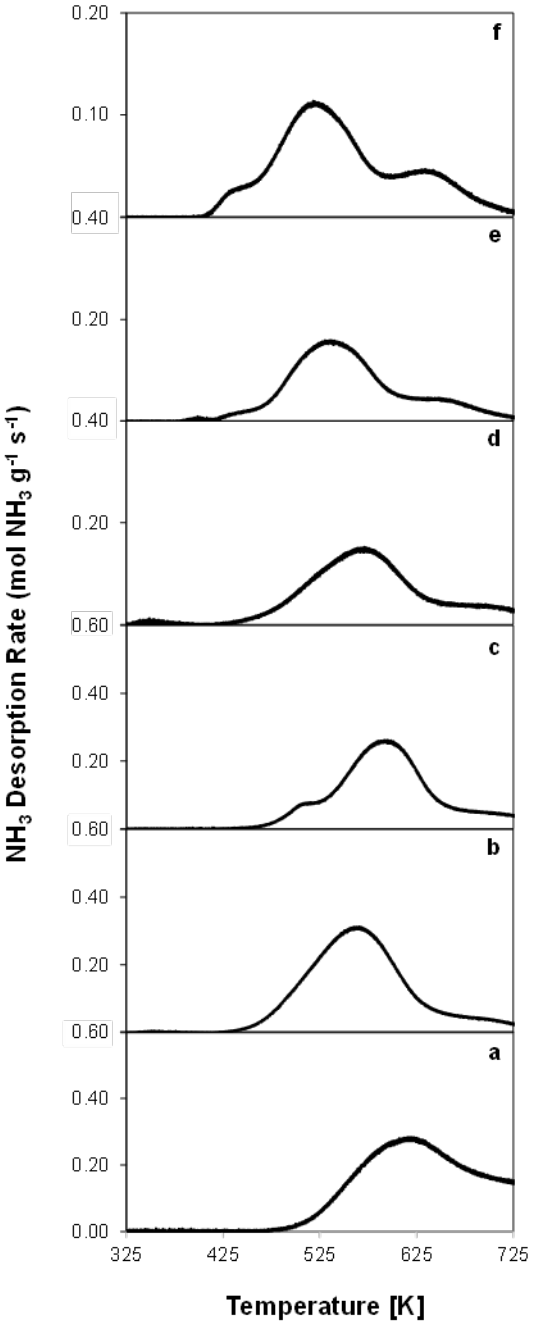


**Figure S12.** $NH_3$ TPD profiles on $NH_4$-form MFI samples synthesized with only $TPA^+$ as the SDA. (a) MFI-TPA(37,0), (b) MFI-TPA(50,0), (c) MFI-TPA(71,0), (d) MFI-TPA(118,0), (e) MFI-TPA(159,0), (f) MFI-TPA(185,0).

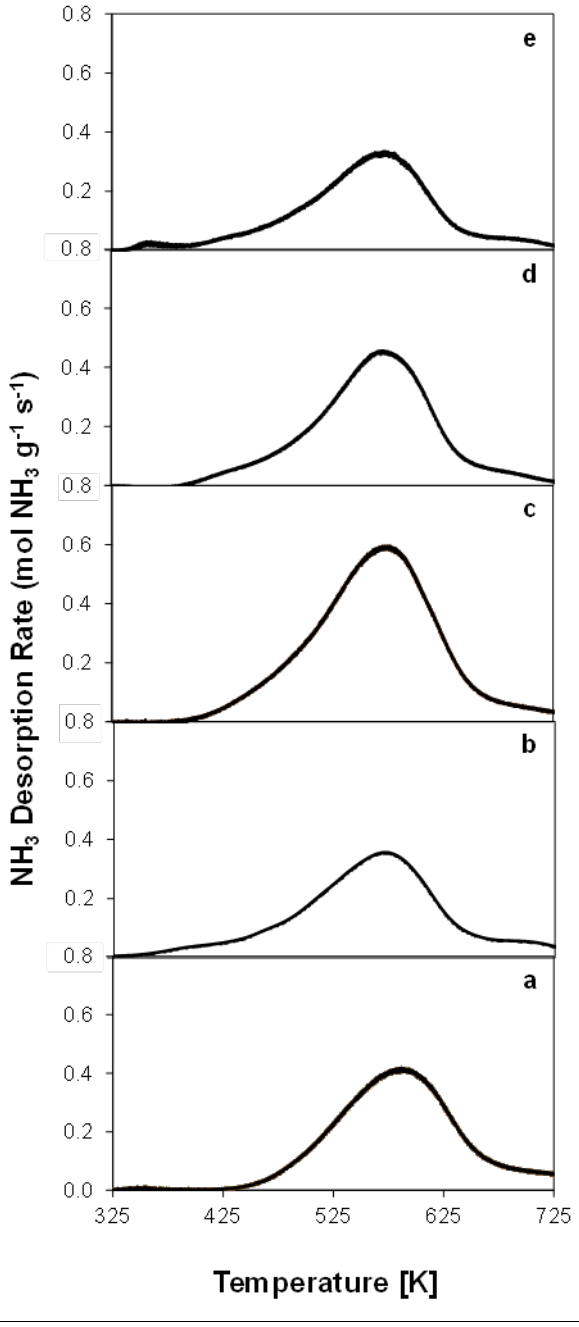


**Figure S13**. $NH_3$ TPD profiles on $NH_4$-form MFI samples synthesized with $Na^+$ and $TPA^+$. (a) MFI-TPA(52,0.25), (b) MFI-TPA(57,0.75), (c) MFI-TPA(51,1.5), (d) MFI-TPA(58,3), (e) MFI-TPA(55,5).

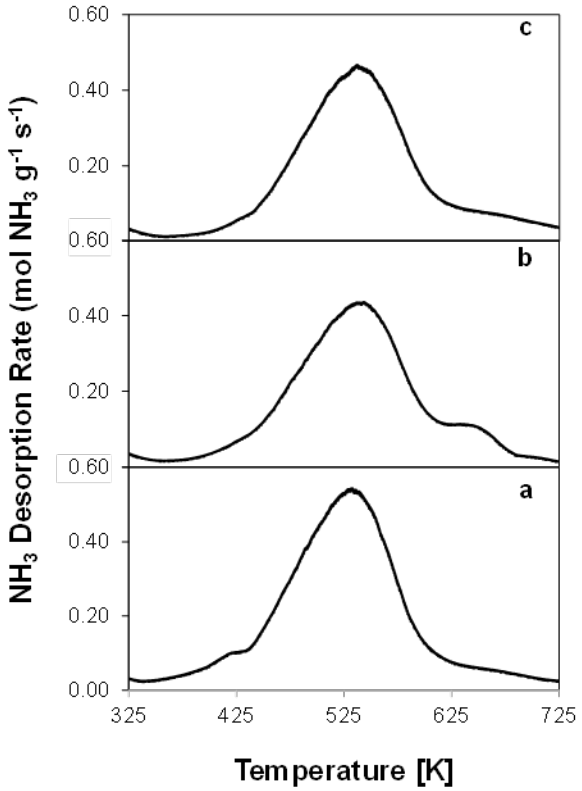


**Figure S14.** $NH_3$ TPD profiles on $NH_4$-MFI samples synthesized with neutral OSDAs. (a) MFI-PETP(43,0.5), (b) MFI-DABCO(44,0.04)-1, (c) MFI-DABCO(44,0.04)-2.

**Section S5. TGA profiles of as-made MFI samples**

The weight loss in the second temperature ramp (523−1073 K) was measured for each sample, and listed in Table S2. This weight loss was attributed to the combustion of organic molecules, and was converted to a molar ratio of $TPA^+$ (186.36 g/mol ), PETP (136.15 g/mol), or DABCO (112.17 g/mol) per MFI unit cell (96 T-atoms; 5769.09 g/mol), according to the following equations:

$$96 = \frac{mol\ Si}{mol\ unit\ cell} + \frac{mol\ Al}{mol\ unit\ cell} \quad \text{(S1)}$$

$$\frac{mol\ OSDA}{mol\ unit\ cell} = \frac{mol\ OSDA/g_{catalyst}}{mol\ Al\ /g_{catalyst}} \frac{mol\ Al}{mol\ unit\ cell} \quad \text{(S2)}$$

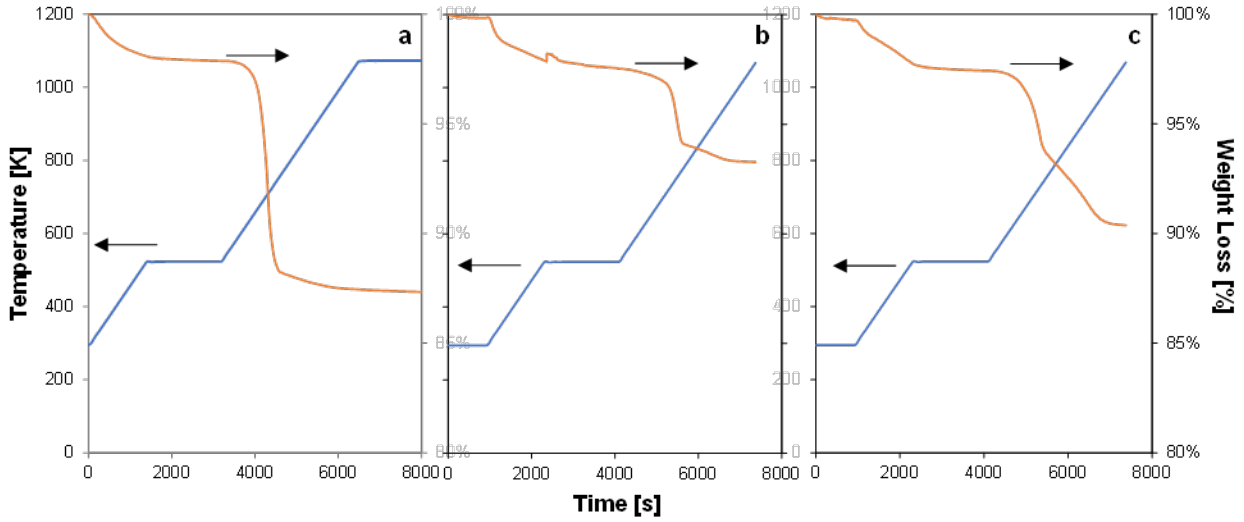


**Figure S15.** Representative TGA profiles on (a) MFI-TPA(58,3), (b) MFI-PETP(43,0.5), and (c) MFI-DABCO(44,0.4)-2.

**Table S2.** Weight loss from combustion of organics from MFI samples synthesized in this study.

| Sample | Weight Loss % | OSDA per unit cell | OSDA per intersection |
|---|---|---|---|
| MFI-TPA(37,0) | 12.75 | 4.05 | 1.01 |
| MFI-TPA(50,0) | 12.02 | 3.80 | 0.95 |
| MFI-TPA(71,0) | 13.28 | 4.17 | 1.04 |
| MFI-TPA(118,0) | 13.35 | 4.17 | 1.04 |
| MFI-TPA(159,0) | 13.02 | 4.06 | 1.01 |
| MFI-TPA(185,0) | 12.96 | 4.03 | 1.01 |
| MFI-TPA (52,0.25) | 12.15 | 3.98 | 1.00 |
| MFI-TPA(57,0.75) | 11.15 | 3.38 | 0.84 |
| MFI-TPA(51,1.5) | 10.97 | 3.54 | 0.88 |
| MFI-TPA(58,3) | 10.74 | 3.64 | 0.91 |
| MFI-TPA(55,5) | 10.61 | 3.64 | 0.80 |
| MFI-PETP(43,0.5) | 4.57 | 1.95 | 0.49 |
| MFI-DABCO(44,0.04)-1 | 8.40 | 4.24 | 1.06 |
| MFI-DABCO(44,0.04)-2 | 7.33 | 3.69 | 0.92 |

**Section S6. Elemental Content on MFI Samples**

The Al content for each sample is reported as the number of Al per 96 T-site unit cell (n) in Table 1. To determine n, the Al content on H-form samples was measured by elemental analysis (mol Al per g sample), and this number was multiplied by the molar mass of a 96 T-atom MFI unit cell ($Si_{96}O_{192}$ = 5768.09 g $mol_{uc}^{-1}$, which is approximately equivalent to $H_nAl_nSi_{96-n}O_{192}$ given the similar molar mass of Si and (Al+H)). The Si/Al ratio (*x*) in a 96 T-site unit cell is defined as:

$$\frac{Si}{Al} = \frac{96-n}{n} \tag{S3}$$

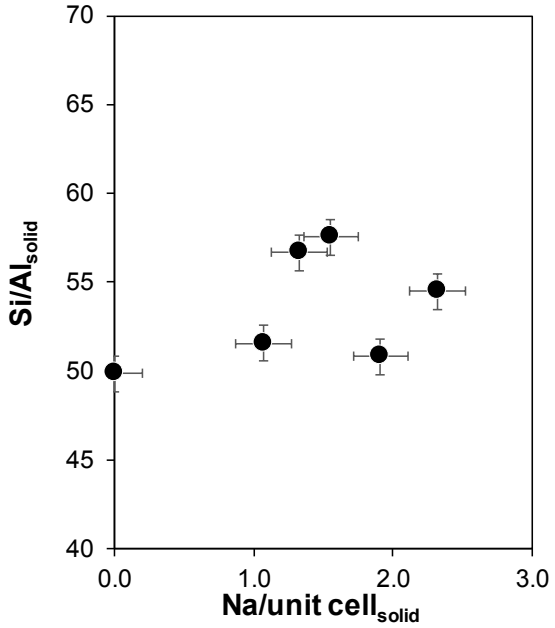


**Figure S16.** Si/Al ratio as a function of the occluded $Na^+$ content on as-made MFI materials (gel Na/TPA = 0–5).

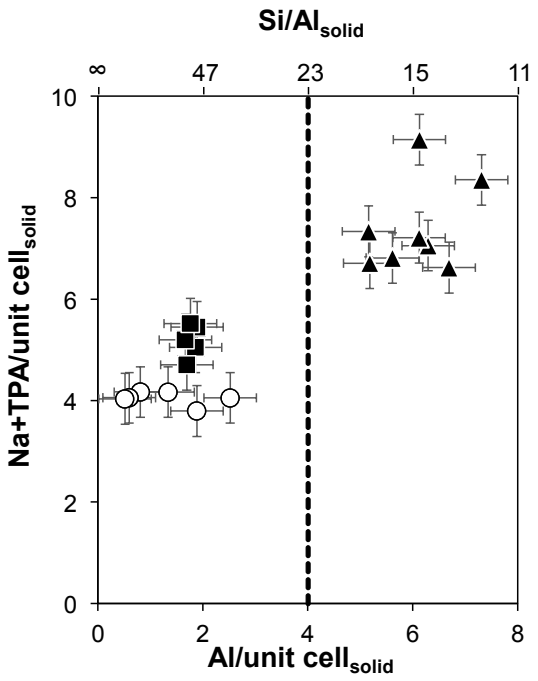


**Figure S17.** The addition of $Na^+$ to the synthesis gel at high Al content results in overcoming the charge density mismatch barrier. MFI samples made only in the presence of $TPA^+$ (○), made with $Na^+$ and $TPA^+$ present at low Al content (gel Si/Al = 50, □) and high Al content (gel Si/Al = 25, ■). Vertical dashed line indicates the theoretical limit of Al per unit cell if only $TPA^+$ (1 per intersection) is used to charge compensate $[AlO_{4/2}]^-$ during synthesis.

**Section S7. Aqueous-Phase $Co^{2+}$ Ion Exchanges of Zeolites**

To study the effects of aqueous-phase ion-exchange procedures on the number and identity of the Co species formed on MFI zeolites, a series of Co-form MFI samples were prepared from the Na-form MFI(13,C) parent sample with varying temperature, $Co(NO_3)_2$ solution molarity, and number of repeat exchanges (holding constant 150 g solution per gram solid). All samples are listed in Table S.3, with a sample code Co-MFI-X-Y-Z, where X denotes the temperature in K, Y denotes the solution molarity in M, and Z denotes the number of repeat exchanges performed.

Initial $Co^{2+}$ ion-exchange experiments performed at ambient temperature (ca. 298 K) for 24 hours using aqueous $Co(NO_3)_2$, which is a commonly reported procedure,[1–5] resulted in an amount of exchanged $Co^{2+}$ that showed a weak dependence on $Co(NO_3)_2$ molarity (Fig. S18a, filled blue circles). At first glance, such data would suggest that $Co^{2+}$ saturation is achieved beyond 0.10 M $Co(NO_3)_2$; however, sequential exchanges of Co-MFI samples with a fresh aqueous $Co(NO_3)_2$ solution (0.25 or 0.5 M) resulted in systematic increases to the Co content on the solid samples recovered after the ion-exchange procedure (Fig. S18a, open blue circles). These findings indicate that Co-form MFI samples did not equilibrate with aqueous $Co(NO_3)_2$ ion-exchange solutions at ambient temperature (ca. 298 K).

$Co^{2+}$ ion-exchange experiments performed at 353 K also showed Langmuirian behavior (Fig S18b, filled red squares), similar to ion-exchange experiments performed at ambient temperature, but surprisingly approached different saturation levels ($Co^{2+}/Al_{tot}$ = 0.07 at ca. 298 K and 0.17 at 353 K). Repeat exchange experiments performed at 353 K at 0.5 M did not further increase $Co^{2+}$ content (Fig. S18b, open red squares), in sharp contrast to analogous experiments

performed at ambient temperature (Fig. S18a), indicating that $Co^{2+}$ saturation of available binding sites is achieved from ion-exchange performed at 353 K.

**Table S3.** Elemental analysis for Na-form MFI(13,C) exchanged with $Co(NO_3)_2$ for 24 hours denoted "Co-MFI(X,Y,Z)", where X denotes the temperature in K, Y denotes the solution molarity in M, and Z denotes the number of repeat exchanges performed (quantities shown in Fig. S18). Adapted from Hur et al.[6]

| Sample Name | $Co/Al_{tot}$ |
|---|---|
| Co-MFI(298,0.001,1) | 0.04 |
| Co-MFI(298,0.005,1) | 0.05 |
| Co-MFI(298,0.05,1) | 0.04 |
| Co-MFI(298,0.05,3) | 0.06 |
| Co-MFI(298,0.05,5) | 0.07 |
| Co-MFI(298,0.25,1) | 0.07 |
| Co-MFI(298,0.25,3) | 0.14 |
| Co-MFI(298,0.25,5) | 0.14 |
| Co-MFI(298,0.25,7) | 0.15 |
| Co-MFI(298,0.25,8) | 0.16 |
| Co-MFI(298,0.50,1) | 0.07 |
| Co-MFI(298,0.50,1) | 0.08 |
| Co-MFI(298,0.50,2) | 0.10 |
| Co-MFI(298,0.50,3) | 0.11 |
| Co-MFI(298,0.50,4) | 0.13 |
| Co-MFI(298,0.50,5) | 0.14 |
| Co-MFI(353,0.001,1) | 0.06 |
| Co-MFI(353,0.005,1) | 0.12 |
| Co-MFI(353,0.05,1) | 0.10 |
| Co-MFI(353,0.25,1) | 0.14 |
| Co-MFI(353,0.50,1) | 0.17 |
| Co-MFI(353,0.50,1) | 0.17 |
| Co-MFI(353,0.50,2) | 0.17 |
| Co-MFI(353,0.50,3) | 0.16 |
| Co-MFI(353,0.50,4) | 0.16 |
| Co-MFI(353,0.50,5) | 0.18 |
| Co-MFI(353,0.75,1) | 0.15 |
| Co-MFI(353,1.00,1) | 0.13 |

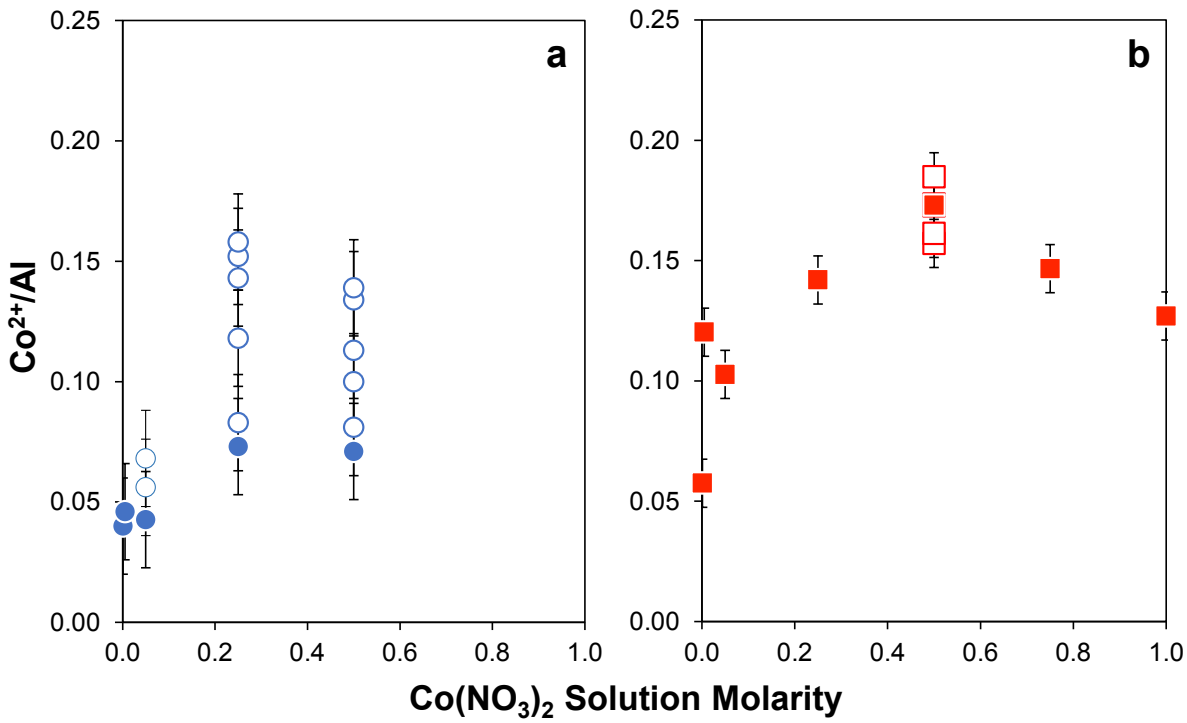


**Figure S18.** The liquid-phase exchange of Na-form MFI(13,C) with $Co(NO_3)_2$ at (a) ambient (ca. 298 K, ▯) and (b) 353 K (■) for a single exchange for 24 hours. Additionally, multiple sequential exchanges (○ for ca. 298 K at 0.05 M, 0.25 M and 0.5 M, respectively, and ▯ for 353 K at 0.5 M, 2-8 repeats) were performed on washed and dried Co-form MFI. Adapted from Hur et al.[6]

The different $Co^{2+}$ saturation uptakes measured on MFI at different temperatures contrast prior reports on CHA, which achieve $Co^{2+}$ saturation at both ambient (ca. 298 K) and elevated (353 K) temperatures at the same $Co^{2+}/Al_{tot}$ values (Fig. S19);[7] this $Co^{2+}$ saturation value has been corroborated independently by $Cu^{2+}$ titration of the same paired Al binding sites (6-MR paired Al) on a suite of CHA samples of varying composition and Al arrangement. Additionally, two MFI samples (MFI-TPA(117,0), MFI-TPA(52,0.25)) were exchanged with a 0.5 M $Co(NO_3)_2$ solution at 353 K, then washed, dried and treated in an high temperature oxidative environment to prepare their saturated Co-form samples; afterward, a second ion-exchange was performed with the same solution that led to saturation (0.5 M $Co(NO_3)_2$, 24 h), but instead at ambient temperature (ca. 298 K). $Co/Al_{tot}$ values on the exchanged MFI samples were similar

before and after the second lower-temperature exchange step, indicating that the additional amounts of $Co^{2+}$ exchanged at elevated temperatures did not reflect weakly bound $Co^{2+}$ species, which should have been removed when Co-form samples were contacted with $Co(NO_3)_2$ solutions at ambient temperature (Table S4).

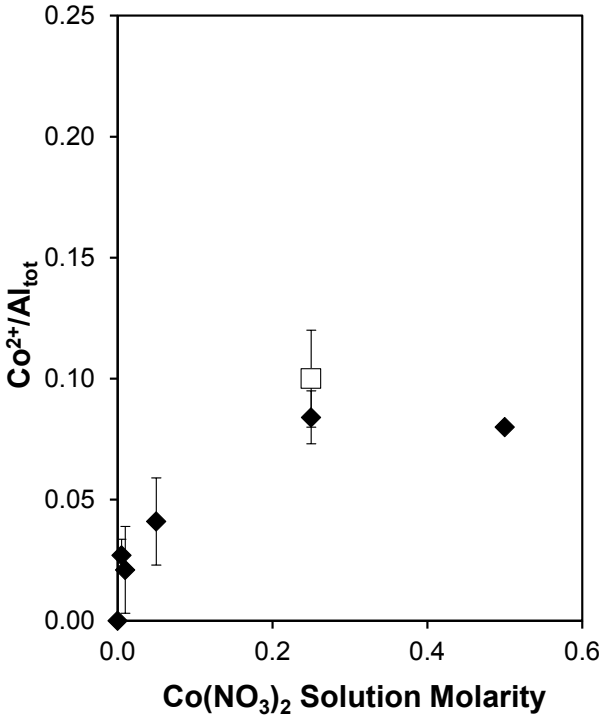


**Figure S19.** $Co^{2+}$ exchange isotherm for H-CHA (Si/Al = 15) at ambient (ca. 298 K, filled ♦), as previously reported by Di Iorio and Gounder,[7] and at 353 K (open □).

**Table S4.** Elemental analysis for two MFI samples exchanged first at 0.5 M $Co(NO_3)_2$ at 353 K for 24 hours, and then exchanged a second time at 0.5 M $Co(NO_3)_2$ at ca. 298 K.

| Sample | $Co/Al_{tot}$ after first exchange (353 K) | $Co/Al_{tot}$ after second exchange (298 K) |
|---|---|---|
| MFI-TPA(117,0) | 0.00 | 0.00 |
| MFI-TPA(52,0.25) | 0.06 | 0.10 |

Additional characterization experiments were performed on Co-MFI samples after dehydration treatments, including those saturated with $Co^{2+}$ at 353 K, to provide evidence for the sole presence of $Co^{2+}$ cations. DRUV-Vis spectra of dehydrated Co-MFI samples in Figure S20a (full UV-Vis spectra in Section S9) showed only absorption bands for d-d transitions of $Co^{2+}$ cations (13,500–23,500 $cm^{-1}$) and no features for cobalt oxides (24,000–28,000 $cm^{-1}$).[8–10] The number of cation sites removed on partially exchanged Co-MFI samples (Co/Na-MFI) was calculated from the residual $Na^+$ retained after $Co^{2+}$-exchange and the number of $H^+$ sites on the parent H-form sample. These residual cation site counts were consistent with the exchange of each $Co^{2+}$ cation at two anionic exchange sites as shown in Figure S20b. First the number of $H^+$ sites on the parent zeolite was determined by $NH_3$ TPD quantification of the $NH_4$-form sample. Then, the Co and Na content were measured on the Co-Na-form. Finally, a $NH_3$ TPD was performed on the Co-Na-form as described in Section 2.3, to quantify the number of residual $H^+$ sites present. The parameter "Sites Removed/Al" depicted in Figure S20b is defined as the number of $Na^+$ and $H^+$ on the Co-Na-form of the sample, subtracted from the number of $H^+$ on the parent form. Theoretically, if only $Co^{2+}$ species are present and each $Co^{2+}$ removed two monovalent cations, then the number of sites removed would increase with Co content with a slope of 2 (dotted line in Figure S20b).

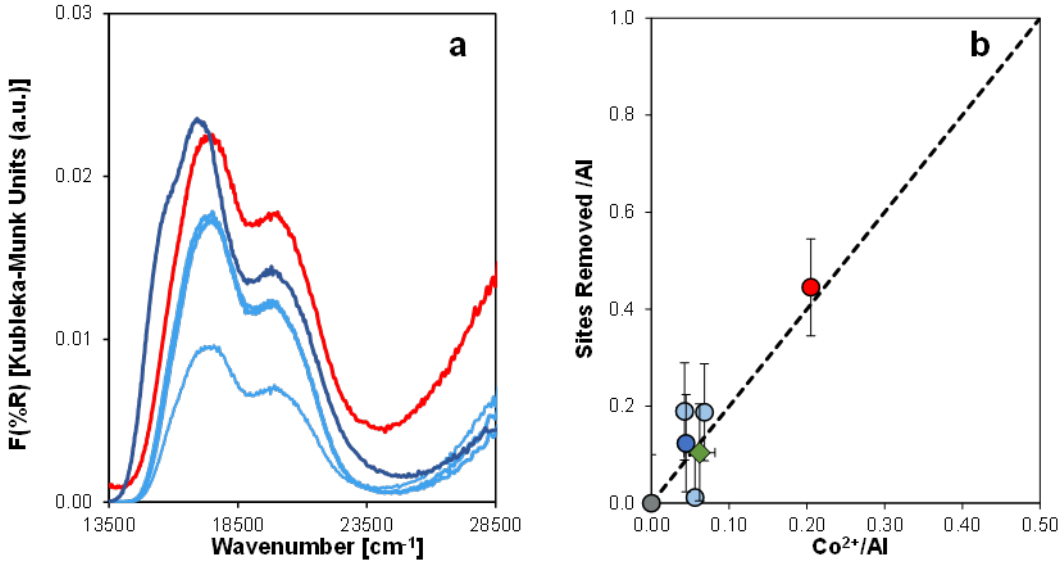


**Figure S20.** (a) Diffuse reflectance UV-visible spectra of partially Co-exchanged MFI(13,C) samples ($Co(NO_3)_2$, 24 h): Co-MFI(298,0.005,1), Co-MFI(298,0.005,3), Co-MFI(298,0.005,5) (light blue), Co-MFI(298,0.50,1) (dark blue), and Co-MFI(353,0.50,1) (red) and (b) total cation exchange sites removed (per Al) on Co-exchanged MFI samples (including the Co-form MFI-TPA(52,0.25) shown as a green diamond). The dashed line corresponds to a slope of 2, which is the stoichiometry expected for 2 $H^+$:1 $Co^{2+}$. Adapted from Hur et al.[6]

**Section S8. UV-Visible Spectra of Co-form Zeolites**

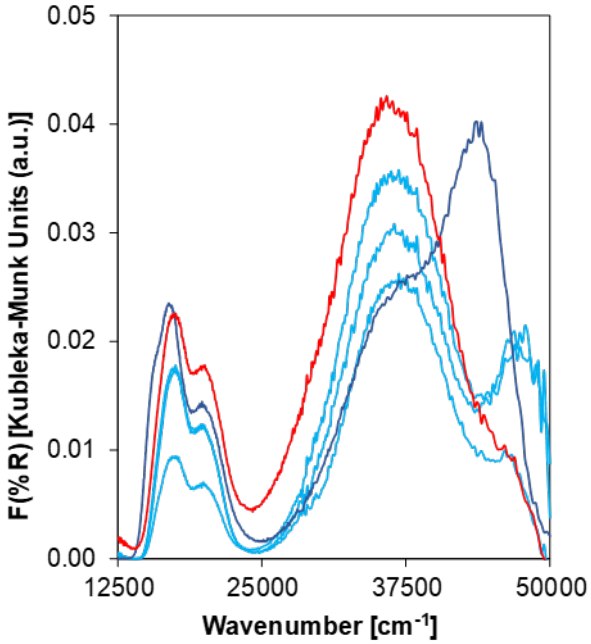


**Figure S21.** Diffuse reflectance UV-visible spectra of dehydrated, partially Co-exchanged MFI samples Co-MFI(298,0.005,1), Co-MFI(298,0.005,3), Co-MFI(298,0.005,5) (light blue), Co-MFI(298,0.50,1) (dark blue), and Co-MFI(353,0.50,1) (red). Adapted from Hur et al.[6]

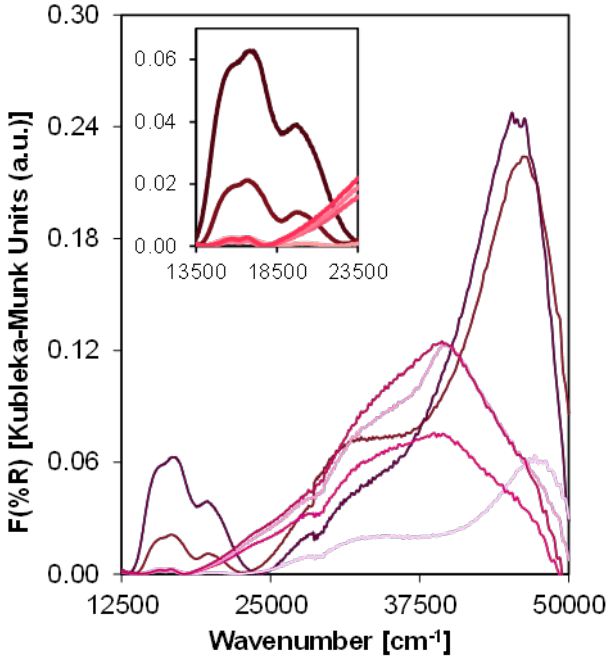


**Figure S22.** Diffuse reflectance UV-visible spectra of dehydrated Co-MFI for parent samples crystallized only in the presence of $TPA^+$ as a function of framework Al content (MFI-TPA(X,0)). Systematically darker colors indicate higher $Co/Al_{tot}$ values. Inset: d-d transition region of Co-MFI samples.

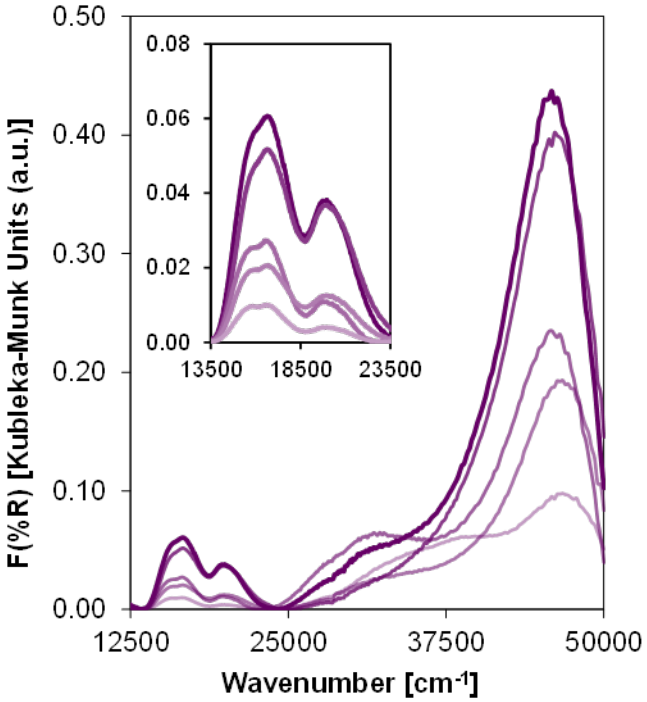


**Figure S23.** Diffuse reflectance UV-visible spectra of dehydrated Co-MFI for parent samples crystallized with constant Al content and varying Na/TPA ratios in synthesis (MFI-TPA(~50, Y)). Systematically darker colors indicate higher $Co/Al_{tot}$ values. Inset: d-d transition region of Co-MFI samples.

## Section S9. MFI O-atom environments

**Table S5.** The indices of O-atoms used in this work, and the corresponding index from the reference from which the MFI structure in this work was constructed, the T-sites bound to each O-atom, and the void environment to which each O-atom belongs.

| **O-atom** | | **O-atom void environment**[c] | | | **T-atoms bound to O-atom** | |
|---|---|---|---|---|---|---|
| This work[a] | van Koningsveld et. al.[b] | Int. | Str. | Sin. | | |
| O1 | O21 | | | | T1 | T5 |
| O2 | O1 | | | | T1 | T2 |
| O3 | O15 | | | | T1 | T10 |
| O4 | O16 | | | | T1 | T4 |
| O5 | O2 | | | | T2 | T3 |
| O6 | O13 | | | | T2 | T8 |
| O7 | O6 | | | | T2 | T6 |
| O8 | O20 | | | | T3 | T12 |
| O9 | O3 | | | | T3 | T4 |
| O10 | O19 | | | | T3 | T6 |
| O11 | O17 | | | | T4 | T7 |
| O12 | O4 | | | | T4 | T5 |
| O13 | O5 | | | | T5 | T6 |
| O14 | O14 | | | | T5 | T11 |
| O15 | O18 | | | | T6 | T9 |
| O16 | O22 | | | | T7 | T11 |
| O17 | O7 | | | | T7 | T8 |
| O18 | O23 | | | | T7 | T7 |
| O19 | O8 | | | | T8 | T9 |
| O20 | O12 | | | | T8 | T12 |
| O21 | O25 | | | | T9 | T9 |
| O22 | O9 | | | | T9 | T10 |
| O23 | O26 | | | | T10 | T10 |
| O24 | O10 | | | | T10 | T11 |
| O25 | O11 | | | | T11 | T12 |
| O26 | O24 | | | | T12 | T12 |

[a] From the numbering assigned by the International Zeolite Association (IZA).[11]
[b] From van Koningsveld, et. al.,[12] the source of the MFI structure used in this work.
[c] Intersection (int.), straight channel (str.), and sinusoidal channel (str.) void environments are denoted here for each O-atom based on the accessible locations around the atom and its ability to catalyze reactions in those environments.

## Section S10. DFT Calculations of TPA-form structures with 1–2 Al in MFI Unit Cell

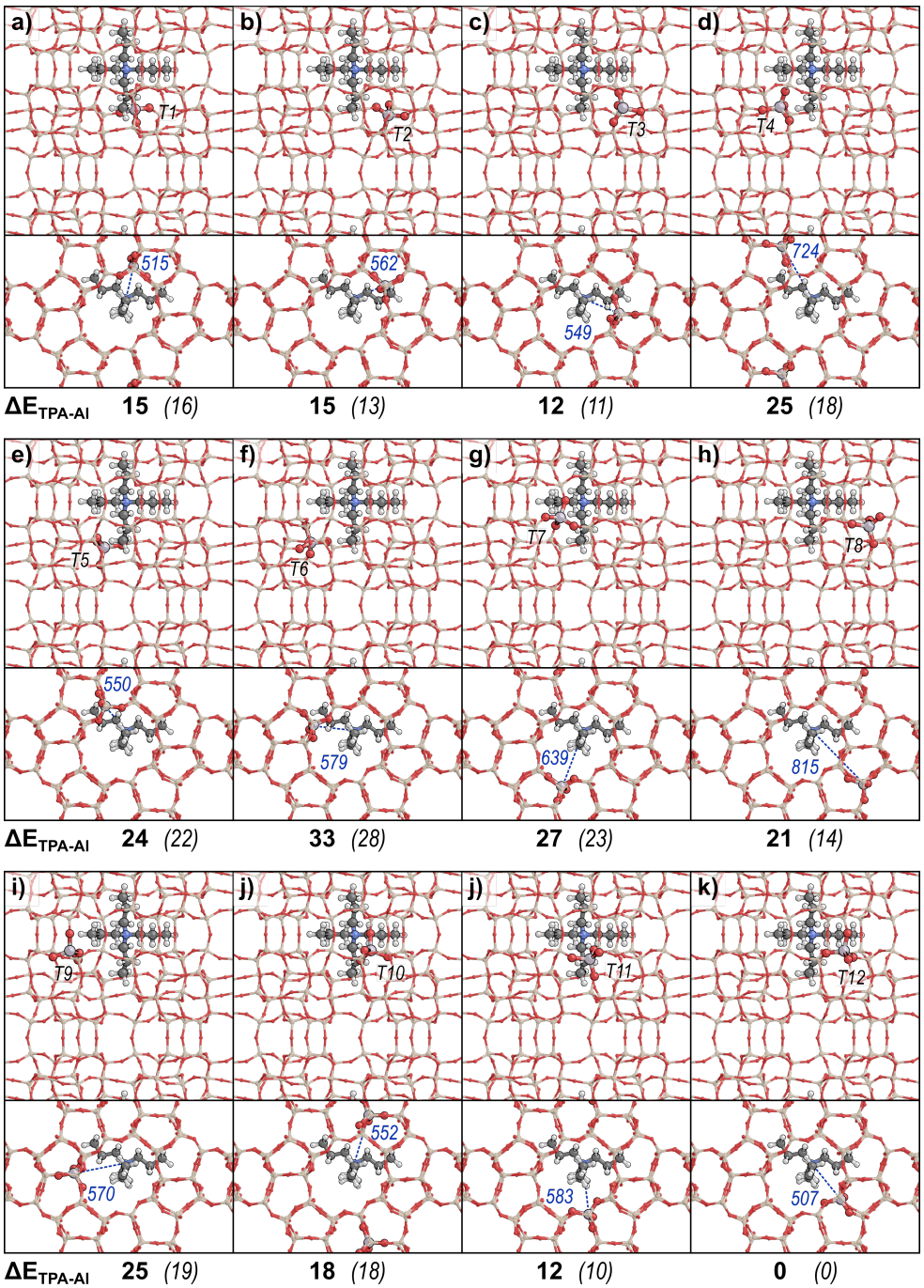


**Figure S24.** The most stable structures with one $TPA^+$ in the MFI unit cell without solvation and Al positioned at each symmetrically unique T-site shown down the *c*-vector (top) and down the *b*-vector (bottom). Relative energies for each configuration are shown beneath each structure in kJ $mol^{-1}$ for structures without solvation (bold) and with solvation (ε = 80; in parentheses and italicized). Blue dashed lines show the path from the N of the $TPA^+$ to the framework Al with distances labeled in pm.

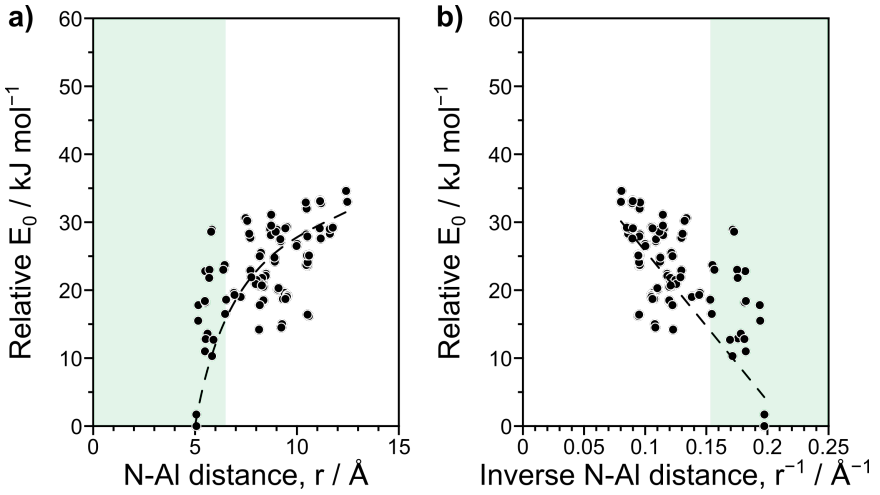


**Figure S25.** The relative energy of MFI with one $TPA^+$ and one Al in the unit cell ($\Delta E_{\text{TPA-Al}}$) with solvation (ε = 80), where Al is substituted at each of the 96 T-site locations as a function of (a) the distance between the N of the $TPA^+$ and the Al of the framework and (b) the inverse of this distance. Green boxes indicate a 6.5 Å cutoff distance and dashed lines are to guide the eye.

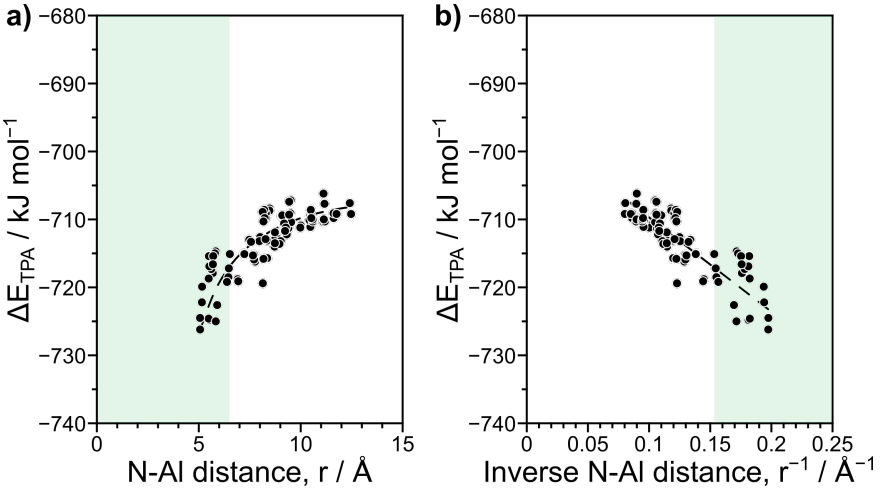


**Figure S26.** $TPA^+$ binding energies ($\Delta E_{TPA}$, Eq. 4, main text) with solvation (ε = 80) as a function of (a) the distance between the N of the $TPA^+$ and the Al of the framework and (b) the inverse of this distance. Green boxes indicate a 6.5 Å cutoff distance and dashed lines are to guide the eye.

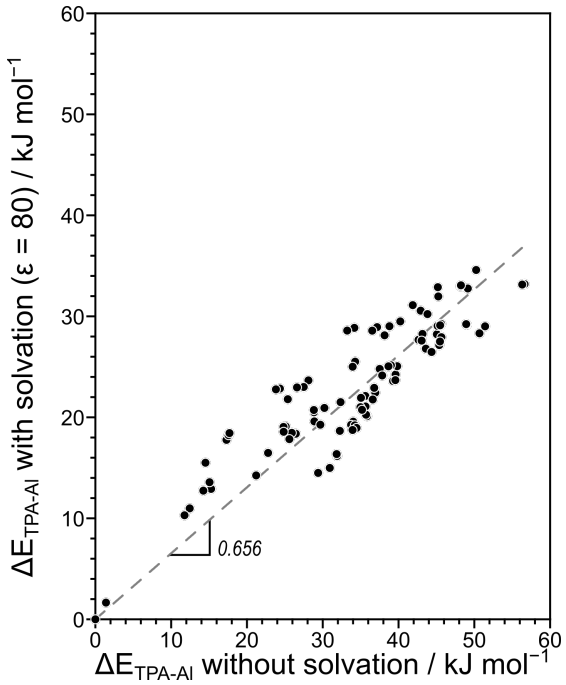


**Figure S27.** Relative energies for TPA-form structures with one Al in the unit cell ($\Delta E_{TPA\text{-}Al}$) with ($\varepsilon = 80$) and without solvation. The dashed line represents a linear fit to the data with its slope labeled in black.

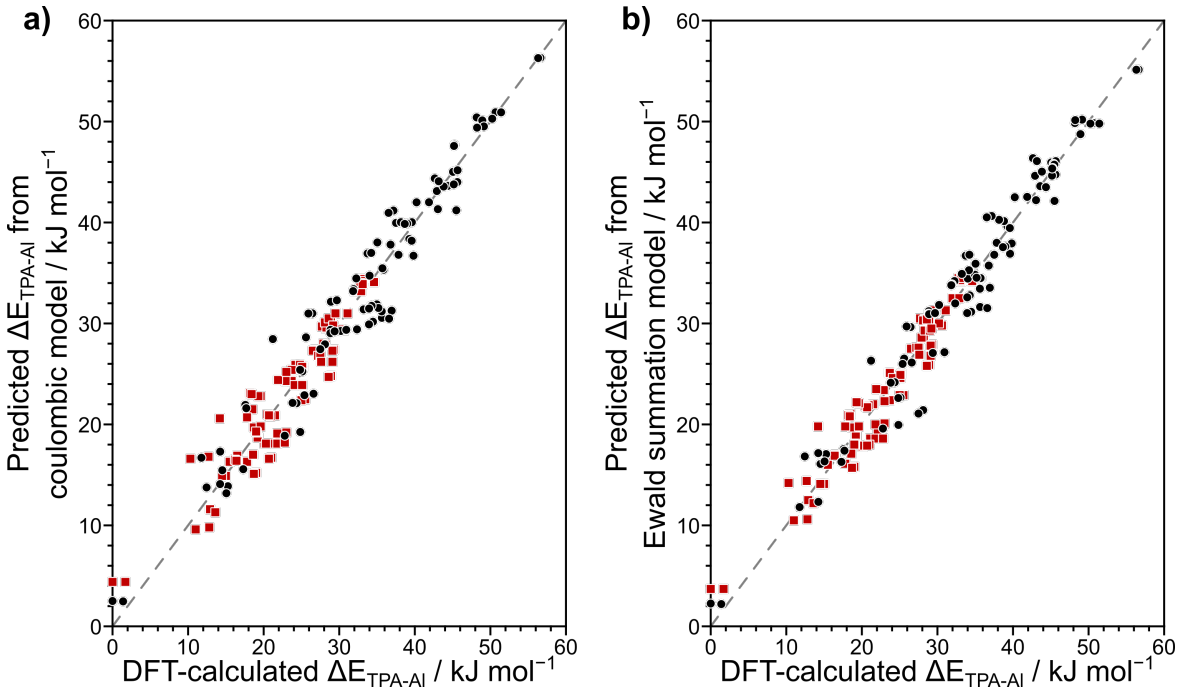


**Figure S28.** Parity plots showing (a) the predicted TPA-form energy based on a coulombic model of interactions between N and Al (Eq. 6, main text) and (b) the predicted TPA-form energy based on an Ewald summation for interactions between N and Al (Eq. 7, main text) as functions of DFT-calculated TPA-form energy ($\Delta E_{TPA\text{-}Al}$) without solvation (●, black) and with solvation ($\varepsilon = 80$; ■, red).

Figure S29 shows the relative Al exchange energies ($\Delta E_{2TPA\text{-}Al}$) for the most stable configurations of $TPA^+$ and $[AlO_{4/2}]^-$ at each unique set of T-sites. Two Al at T12 sites (T12-T12) with $TPA^+$ in adjacent intersections adjoined by a sinusoidal pore (Fig. 4b, main text) is the most stable 2 TPA-Al configuration (Fig. S29). Furthermore, the most stable configuration of two sites for each other T-site contains one Al at T12 (e.g., the most stable configuration containing T1 is a T1-T12 combination). The average energy of each preferred site combination containing a T12 site (i.e., the average of the best T1-T12 combination, T2-T12 combination, etc.) is 14 kJ $mol^{-1}$. Site combinations containing T2 and T8 are also relatively stable, with average relative energies of 21 and 27 kJ $mol^{-1}$, and generally for the second most stable configurations for two Al. These relative Al exchange energies indicate that the behavior of the

single TPA-Al system applies to $TPA_2$-$Al_2$ systems as well; T12 is consistently the most favorable Al atom location, but not prohibitively so, caused by the intrinsic preference of Al to site in that crystallographic location and its proximity to the center of the intersections within which $TPA^+$ resides.

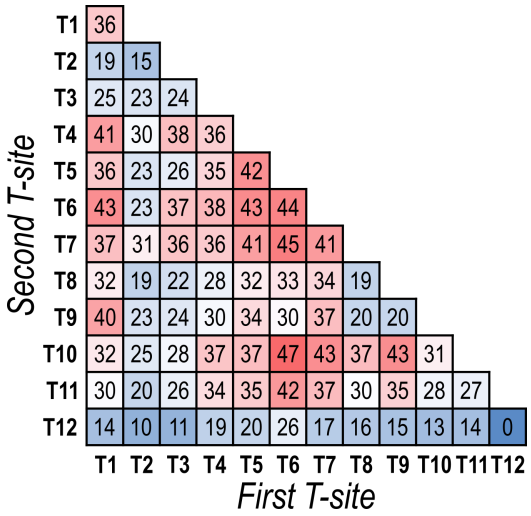


**Figure S29.** The relative energies of the most stable pair of T-sites formed with 2 $TPA^+$ in the unit cell. The T-site with a lower index is labeled on the bottom and the second site on the left.

**Section S11. DFT-calculated Co-exchange in CHA and MFI**

Liquid phase Co-exchange occurs from $Co^{2+}(H_2O)_6$ in solution instead of directly from $Co(NO_3)_2$. The choice of the gas-phase species from which exchange energies are calculated, however, is arbitrary. If Co-exchange energies were calculated instead relative to $Co^{2+}(H_2O)_6$ and formed a gas-phase proton, the new exchange energy would be:

$$\Delta E'_{Co-exch} = 2E[\mathrm{H^+(g)}] + 6E[\mathrm{H_2O(g)}] + E[\mathrm{CoZ_2}] - E[\mathrm{Co^{2+}(H_2O)_6(g)}] - \langle E[(\mathrm{HZ})_2]\rangle \quad \text{(S4)}$$

This form of the exchange energy can be converted to that used in the main text ($\Delta E_{Co\text{-}exch}$, Eq. 3) by a simple constant, which is the difference between these two exchange energy values, $\Delta\Delta E'_{Co\text{-}exch}$:

$$\Delta\Delta E'_{Co-exch} = 2E[\mathrm{H^+(g)}] + 6E[\mathrm{H_2O(g)}] + E[\mathrm{Co(NO_3)_2(g)}] - E[\mathrm{Co^{2+}(H_2O)_6(g)}] - 2E[\mathrm{HNO_3(g)}] \quad \text{(S5)}$$

$$\Delta\Delta E'_{Co-exch} = 1698\ \mathrm{kJ\ mol^{-1}} \quad \text{(S6)}$$

This constant, if added to $\Delta E_{Co\text{-}exch}$ values in the text, would yield Co-exchange energies relative to the $Co^{2+}(H_2O)_6$ complex present in solution; however, the difference between these energies ultimately indicates the preference for Co titration. Similarly, exchange energies can be calculated relative to a bare $Co^{2+}$ cation in the gas phase, for which the difference in energy relative to those calculated in the main text is:

$$\Delta\Delta E''_{Co-exch} = 2E[\mathrm{H^+(g)}] + E[\mathrm{Co(NO_3)_2(g)}] - E[\mathrm{Co^{2+}(g)}] - 2E[\mathrm{HNO_3(g)}] \quad \text{(S7)}$$

$$\Delta\Delta E''_{Co-exch} = 192\ \mathrm{kJ\ mol^{-1}} \quad \text{(S8)}$$

Below, we show four Co-form CHA structures, with $Co^{2+}$ in the two possible Al-Al configurations in a 6-MR (NNN and NNNN; Fig. S30a-b), the Al-Al structure with the lowest $\Delta E_{Co\text{-}exch}$ of any pair sharing an 8-MR (8-MR NNN, Fig. S30c), and the Al-Al structure with the

lowest $\Delta E_{Co\text{-}exch}$ of any pair sharing the di-6-MR of CHA (Fig. S30d). These structures were used to benchmark $Co^{2+}$-exchange energies in MFI.

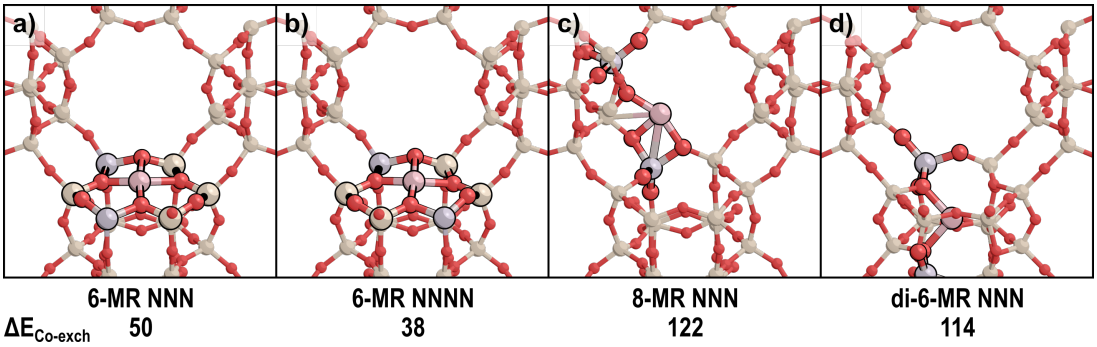


**Figure S30.** Al-Al pairs in CHA with the lowest $Co^{2+}$-exchange energies ($\Delta E_{Co\text{-}exch}$) for two Al in (a) an NNN configuration sharing a 6-MR, (b) an NNNN configuration sharing a 6-MR, (c) an NNN configuration sharing an 8-MR, and (d) an NNN configuration sharing the di-6-MR. $Co^{2+}$-exchange energies ($\Delta E_{Co\text{-}exch}$) are shown below each structure in kJ $mol^{-1}$.

**Table S6.** The minimum, maximum, and average $\Delta E_{Co\text{-}exch}$ values for each unique 4-, 5-, and 6-MR in MFI.

| Ring T-sites | Ring Size | Unique Al-Al Structures[a] | | | Average $\Delta E_{Co\text{-}exch}$ (kJ mol$^{-1}$) | Environment[b] |
|---|---|---|---|---|---|---|
| | | Total | $\Delta E_{Co\text{-}exch}$ < 60 kJ mol$^{-1}$ | $\Delta E_{Co\text{-}exch}$ = 60–90 kJ mol$^{-1}$ | | |
| T9-T9-T10-T10 | 4 | 1 | 0 | 1 | 77 | Sinusoidal |
| T1-T2-T3-T4-T6 | 5 | 3 | 2 | 1 | 54 | Inaccessible |
| T1-T2-T4-T7-T8 | 5 | 3 | 2 | 1 | 52 | Straight |
| T1-T2-T6-T9-T10 | 5 | 5 | 4 | 1 | 51 | Sinusoidal |
| T1-T4-T5-T10-T11 | 5 | 5 | 5 | 0 | 47 | Inaccessible |
| T1-T4-T5-T7-T11 | 5 | 3 | 2 | 1 | 53 | Straight |
| T2-T3-T4-T5-T6 | 5 | 5 | 2 | 3 | 72 | Sinusoidal |
| T2-T3-T6-T8-T12 | 5 | 3 | 2 | 1 | 61 | Inaccessible |
| T2-T3-T6-T8-T9 | 5 | 5 | 0 | 5 | 75 | Straight |
| T3-T4-T7-T8-T12 | 5 | 5 | 0 | 4 | 79 | Sinusoidal |
| T3-T5-T6-T11-T12 | 5 | 5 | 2 | 2 | 67 | Straight |
| T8-T9-T10-T11-T12 | 5 | 5 | 3 | 2 | 58 | Inaccessible |
| T1-T1-T4-T4-T5-T5 | 6 | 5 | 4 | 1 | 32 | Inaccessible |
| T1-T2-T5-T7-T8-T11 | 6 | 2 | 0 | 2 | 86 | Straight |
| T1-T3-T4-T6-T9-T10 | 6 | 2 | 1 | 1 | 42 | Inaccessible |
| T1-T4-T5-T7-T10-T11 | 6 | 5 | 3 | 1 | 56 | Intersection |
| T2-T5-T6-T8-T11-T12 | 6 | 2 | 2 | 0 | 37 | Inaccessible |
| T4-T5-T6-T7-T8-T9 | 6 | 1 | 0 | 1 | 84 | Intersection |
| T7-T7-T10-T10-T11-T11 | 6 | 1 | 1 | 0 | 38 | Intersection |
| T7-T7-T11-T11-T12-T12 | 6 | 4 | 1 | 2 | 80 | Intersection |
| T7-T7-T8-T8-T12-T12 | 6 | 2 | 2 | 0 | 46 | Sinusoidal |
| T7-T7-T8-T8-T9-T9 | 6 | 2 | 1 | 1 | 63 | Intersection |
| T8-T8-T9-T9-T12-T12 | 6 | 3 | 2 | 1 | 46 | Intersection |
| T10-T10-T11-T11-T12-T12 | 6 | 3 | 1 | 2 | 59 | Intersection |
| | | 25 | 19 | 6 | 47 | Inaccessible |
| | | 16 | 8 | 6 | 61 | Intersection |
| | | 18 | 6 | 11 | 66 | Straight |
| | | 18 | 8 | 9 | 65 | Sinusoidal |

[a] Number of unique Co-form structures examined in this work.

[b] Environment is defined as the void or channel whose perimeter interfaces with the plane of the ring. Some rings are enclosed entirely within subunits of MFI and do not interface directly with the intersection, straight channel, or sinusoidal channel, which are labeled Inaccessible.

**Table S7.** Number of Al-Al pairs in different configurations where $Co^{2+}$ is likely to exchange ($\Delta E_{Co\text{-}exch}$ <60 kJ $mol^{-1}$), could possibly exchange ($\Delta E_{Co\text{-}exch}$ = 60–90 kJ $mol^{-1}$), or is unlikely to exchange ($\Delta E_{Co\text{-}exch}$ >90 kJ $mol^{-1}$).

| | **NN** | **4-MR** | **5-MR** | **6-MR NNN** | **6-MR NNNN** | **Subunit, no ring** | **10-MR** | **Far** | **Total** |
|---|---|---|---|---|---|---|---|---|---|
| *$\Delta E_{Co\text{-}exch}$ Range (kJ $mol^{-1}$)* | 80–215 | 77 | 29–90 | 32–107 | 5–90 | 52–226 | 102–255 | 130–299 | 5–299 |
| *$\Delta E_{Co\text{-}exch}$ Avg. (kJ $mol^{-1}$)* | 134 | 77 | 61 | 68 | 47 | 120 | 172 | 197 | 119 |
| *Likely* | 0 | 0 | 24 | 6 | 12 | 1 | 0 | 0 | 43 |
| *Possible* | 3 | 1 | 20 | 6 | 7 | 9 | 0 | 0 | 46 |
| *Unlikely* | 23 | 0 | 2 | 2 | 0 | 21 | 19 | 46 | 113 |
| *Total Examined* | 26 | 1 | 46 | 14 | 19 | 31 | 19 | 46 | 202 |

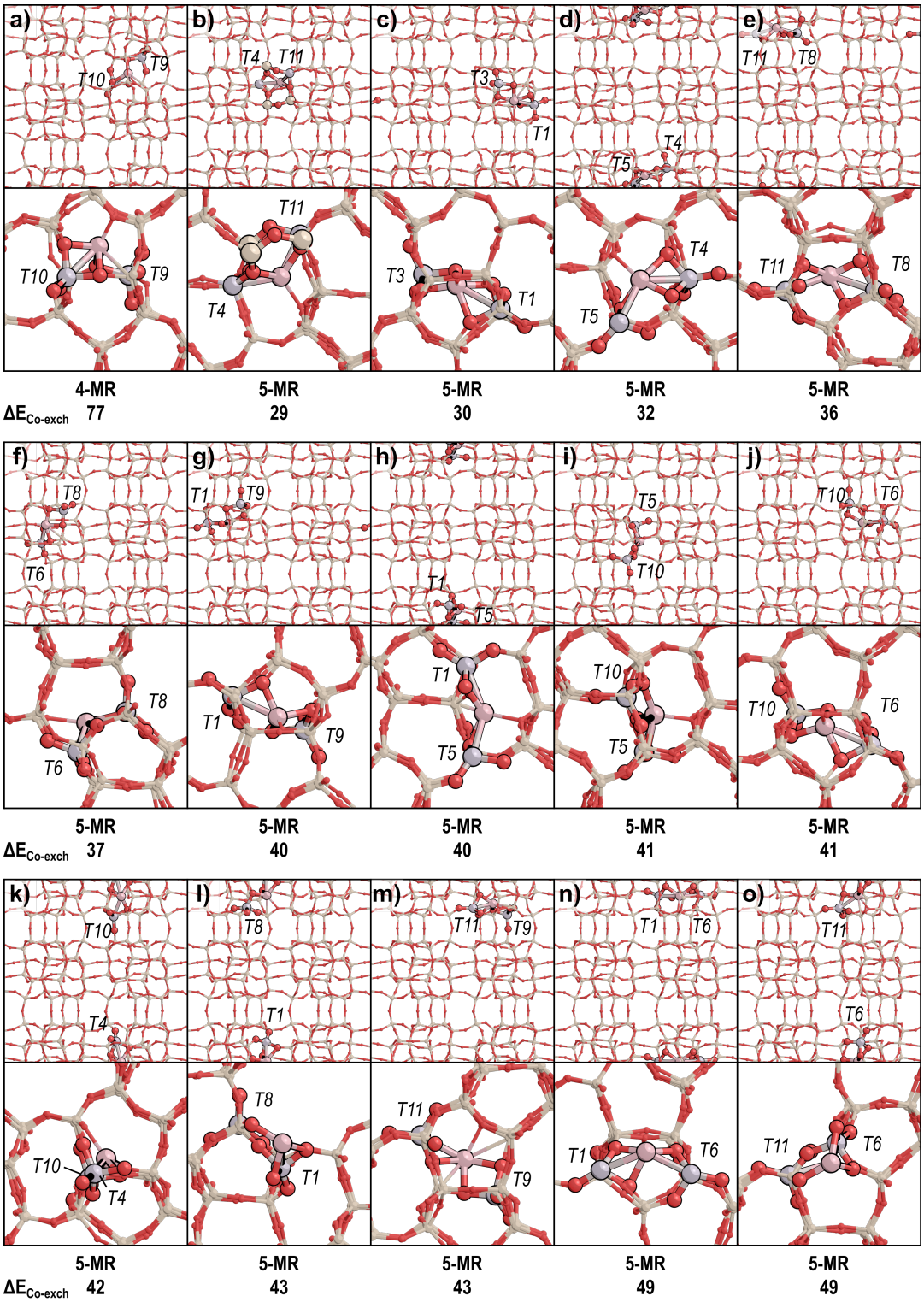


**Figure S31.** Co-form MFI pairs in (a) 4-MR and (b-o) 5-MR configurations with $\Delta E_{Co\text{-}exch} < 50$ kJ mol$^{-1}$. The T-sites at which Al is substituted are labeled in each image and the Co-exchange energies ($\Delta E_{Co\text{-}exch}$) are shown below each structure in kJ mol$^{-1}$.

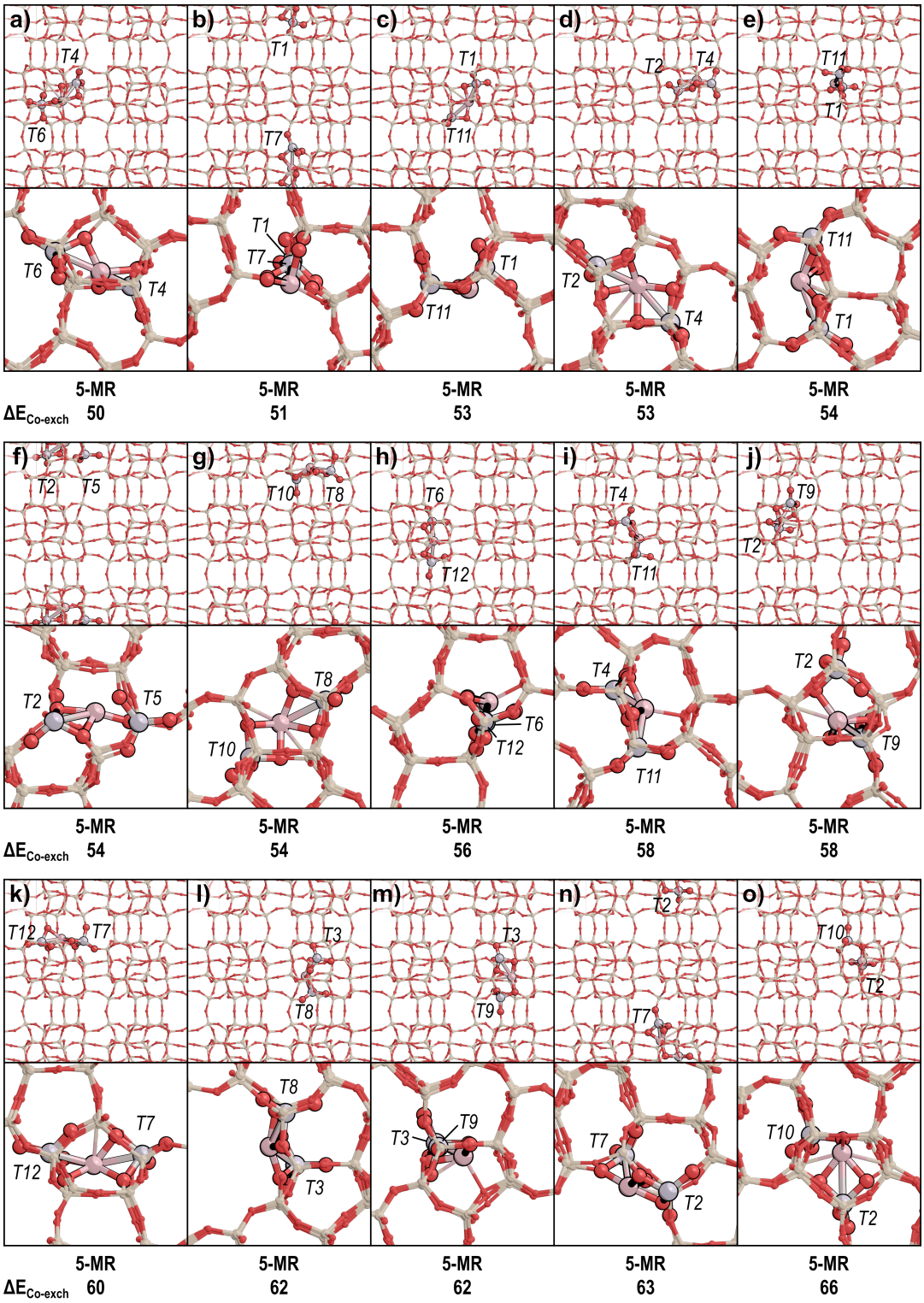


**Figure S32.** Co-form MFI pairs in 5-MR configurations with $\Delta E_{Co\text{-}exch} < 67$ kJ mol$^{-1}$. The T-sites at which Al is substituted are labeled in each image and the Co-exchange energies ($\Delta E_{Co\text{-}exch}$) are shown below each structure in kJ mol$^{-1}$.

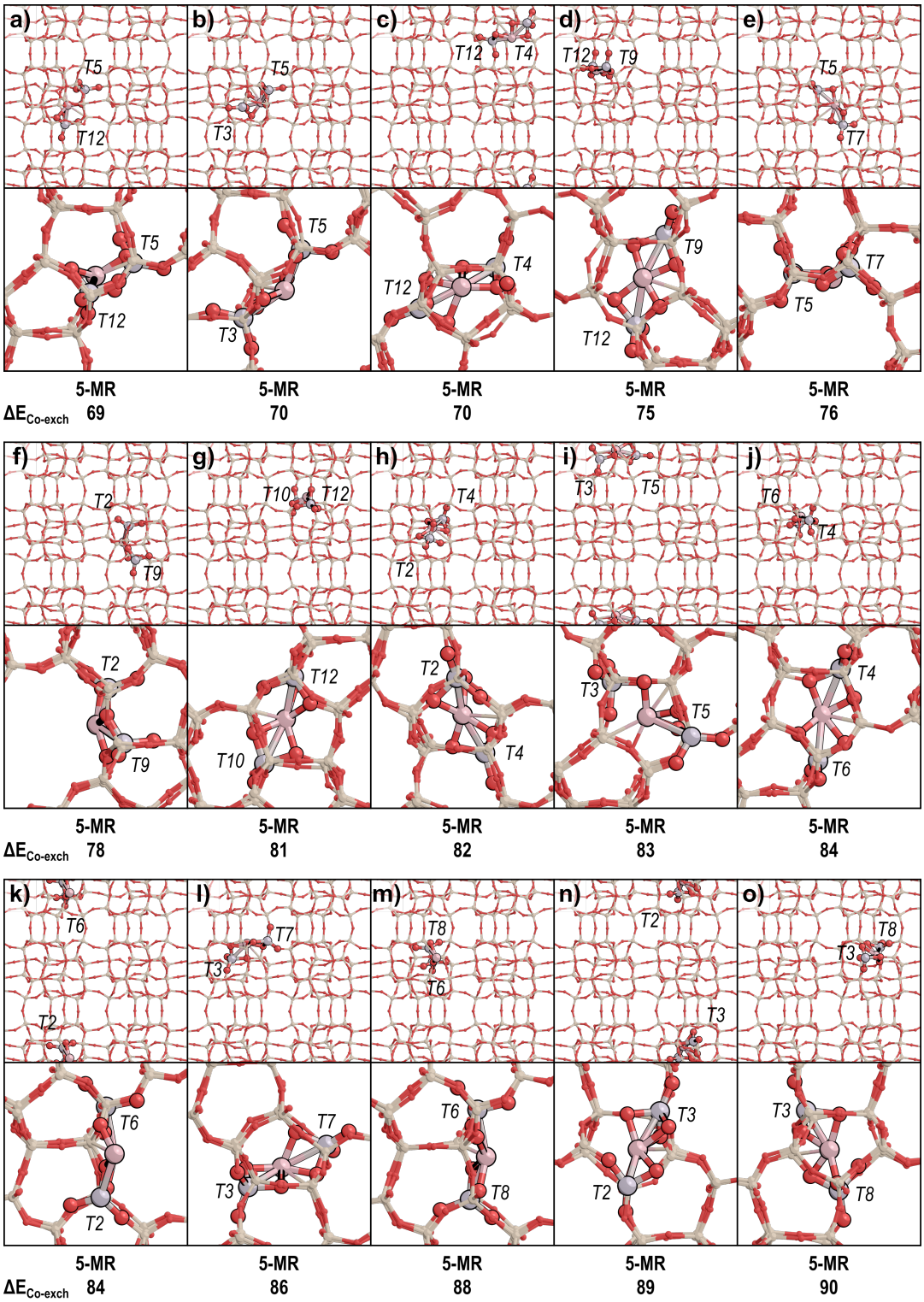


**Figure S33.** Co-form MFI pairs in 5-MR configurations with $\Delta E_{Co\text{-}exch}$ < 90 kJ mol$^{-1}$. The T-sites at which Al is substituted are labeled in each image and the Co-exchange energies ($\Delta E_{Co\text{-}exch}$) are shown below each structure in kJ mol$^{-1}$.

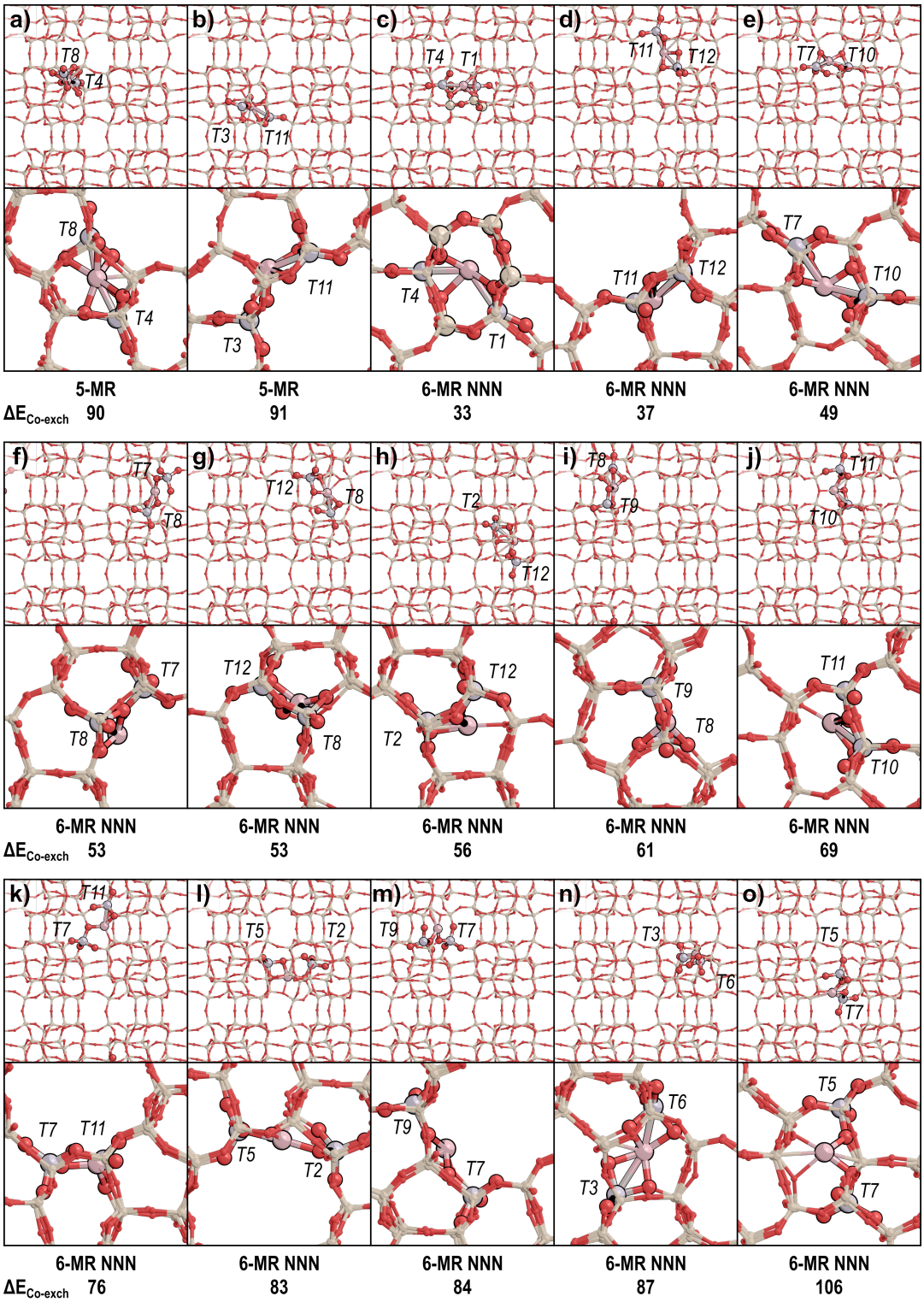


**Figure S34.** Co-form MFI pairs in (a-b) 5-MR with $\Delta E_{Co\text{-}exch}$ > 90 kJ mol$^{-1}$ and (c-o) 6-MR NNN configurations with $\Delta E_{Co\text{-}exch}$ < 107 kJ mol$^{-1}$. The T-sites at which Al is substituted are labeled in each image and the Co-exchange energies ($\Delta E_{Co\text{-}exch}$) are shown below each structure in kJ mol$^{-1}$.

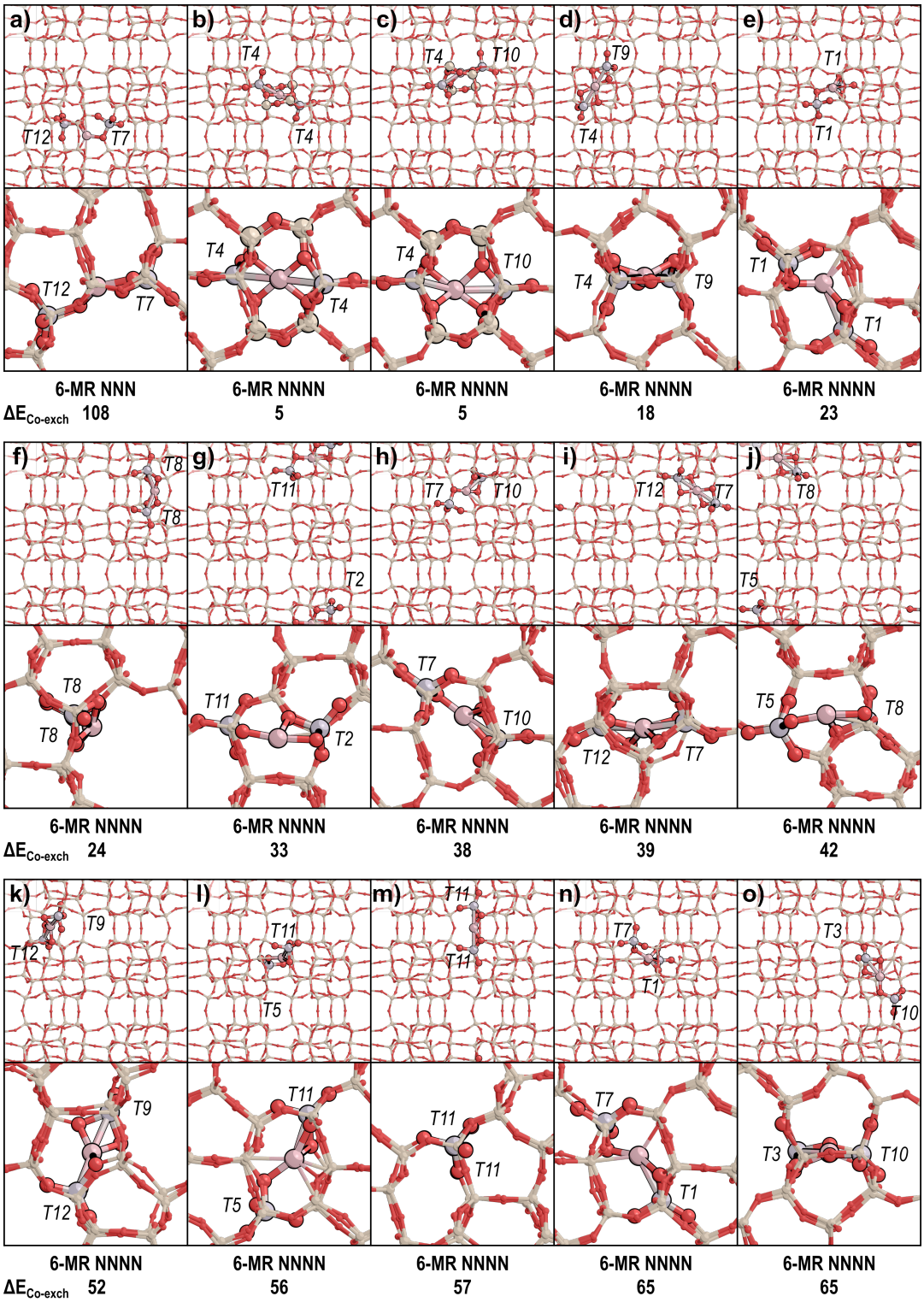


**Figure S35.** Co-form MFI pairs in (a) 6-MR NNN with $\Delta E_{Co\text{-}exch} > 106$ kJ mol$^{-1}$ and (b-o) 6-MR NNNN configurations with $\Delta E_{Co\text{-}exch} < 66$ kJ mol$^{-1}$. The T-sites at which Al is substituted are labeled in each image and the Co-exchange energies ($\Delta E_{Co\text{-}exch}$) are shown below each structure in kJ mol$^{-1}$.

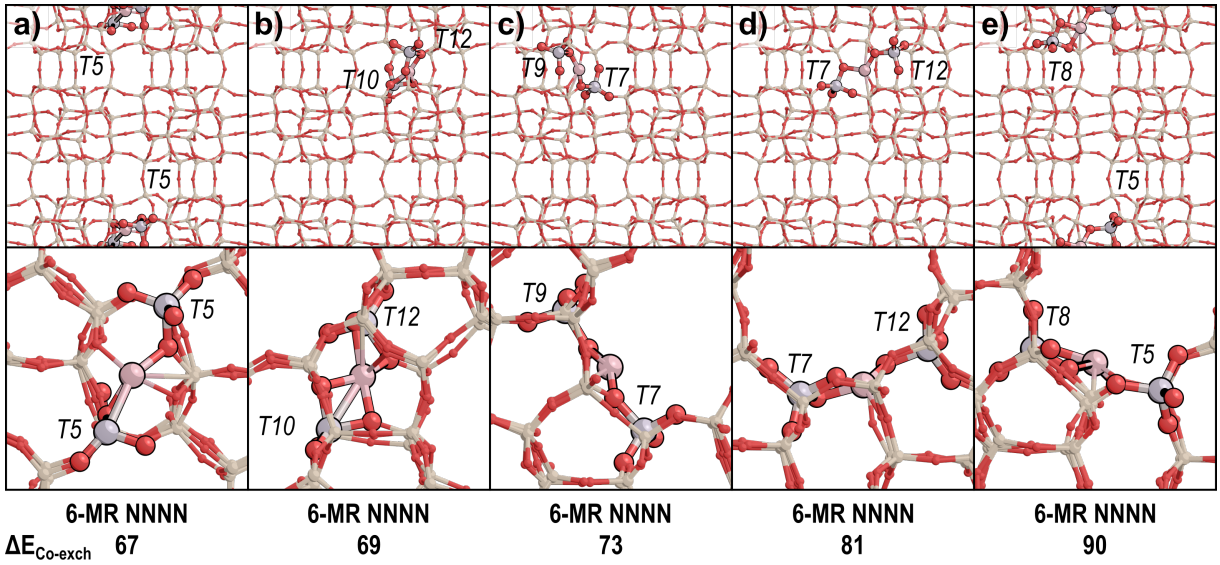


**Figure S36.** Co-form MFI pairs in 6-MR NNNN configurations with $\Delta E_{Co\text{-}exch} > 65$ kJ mol$^{-1}$. The T-sites at which Al is substituted are labeled in each image and the Co-exchange energies ($\Delta E_{Co\text{-}exch}$) are shown below each structure in kJ mol$^{-1}$.

**Section S12. References**


(1) Dědeček, J.; Kaucký, D.; Wichterlová, B. $Co^{2+}$ Ion Siting in Pentasil-Containing Zeolites, Part 3.: $Co^{2+}$ Ion Sites and Their Occupation in ZSM-5: A VIS Diffuse Reflectance Spectroscopy Study. *Microporous Mesoporous Mater.* 2000, *35–36*, 483–494.

(2) Dědeček, J.; Kaucký, D.; Wichterlová, B.; Gonsiorová, O. $Co^{2+}$ Ions as Probes of Al Distribution in the Framework of Zeolites. ZSM-5 Study. *Phys. Chem. Chem. Phys.* 2002, *4* (21), 5406–5413.

(3) Janda, A.; Bell, A. T. Effects of Si/Al Ratio on the Distribution of Framework Al and on the Rates of Alkane Monomolecular Cracking and Dehydrogenation in H-MFI. *J. Am. Chem. Soc.* 2013, *135* (51), 19193–19207.

(4) Pashkova, V.; Klein, P.; Dedecek, J.; Tokarová, V.; Wichterlová, B. Incorporation of Al at ZSM-5 Hydrothermal Synthesis. Tuning of Al Pairs in the Framework. *Microporous Mesoporous Mater.* 2015, *202*, 138–146.

(5) Song, C.; Chu, Y.; Wang, M.; Shi, H.; Zhao, L.; Guo, X.; Yang, W.; Shen, J.; Xue, N.; Peng, L.; Ding, W. Cooperativity of Adjacent Brønsted Acid Sites in MFI Zeolite Channel Leads to Enhanced Polarization and Cracking of Alkanes. *J. Catal.* 2017, *349*, 163–174.

(6) Hur, Y. G.; Kester, P. M.; Nimlos, C. T.; Cho, Y.; Miller, J. T.; Gounder, R. Influence of Tetrapropylammonium and Ethylenediamine Structure-Directing Agents on the Framework Al Distribution in B–Al–MFI Zeolites. *Ind. Eng. Chem. Res.* 2019, *58* (27), 11849–11860.

(7) Di Iorio, J. R.; Gounder, R. Controlling the Isolation and Pairing of Aluminum in Chabazite Zeolites Using Mixtures of Organic and Inorganic Structure-Directing Agents. *Chem. Mater.* 2016, *28* (7), 2236–2247.

(8) Klier, K. Transition-Metal Ions in Zeolites: The Perfect Surface Sites. *Langmuir* 1988, *4* (1), 13–25.

(9) Klier, K. Stereospecific Adsorption of Nitrous Oxide, Cyclopropane, Water, and Ammonia on the Co(II)A Synthetic Zeolite. In *Molecular Sieve Zeolites-I*; Flanigen, E. M., Sand, L. B., Eds.; Advances in Chemistry; American Chemical Society: Washington D.C., 1974; Vol. 101, pp 480–489.

(10) Klier, K.; Kellerman, R.; Hutta, P. J. Spectra of Synthetic Zeolites Containing Transition Metal Ions. V.* Π Complexes of Olefins and Acetylene with Co(II)A Molecular Sieve. *J. Chem. Phys.* 1974, *61* (10), 4224–4234.

(11) Baerlocher, C.; McCusker, L. B. Database of Zeolite Structures http://www.iza-structure.org/databases/ (accessed Jul 31, 2020).

(12) Koningsveld, H. V. High-Temperature (350 K) Orthorhombic Framework Structure of Zeolite H-ZSM-5. *Acta Crystallogr. Sect. B* 1990, *46* (6), 731–735.